Arc-jet wind tunnel characterization of Ultra-High-Temperature Ceramic Matrix Composites

S. Mungiguerra[a]*, G.D. Di Martino[a], A. Cecere[a], R. Savino[a], L. Silvestroni[b], A. Vinci[b], L. Zoli[b], D. Sciti[b]

[a]*University of Naples "Federico II", Department of Industrial Engineering, Aerospace Division, P.le Tecchio 80, 80125 Napoli, Italy*

[b]*National Research Council, Institute of Science and Technology for Ceramics, Via Granarolo 64, 48018 Faenza, Italy*

Abstract

Two samples of Ultra-High-Temperature Ceramic Matrix Composites, with carbon fibers in a ZrB_2-SiC matrix, were exposed to supersonic dissociated air flow, simulating the atmospheric re-entry environment, in an arc-heated facility at specific total enthalpies up to 20 MJ/kg. Surface temperatures, exceeding 2400 K, were monitored by non-intrusive infrared equipment, which allowed detecting thermo-chemical surface instability phenomena. A zirconium oxide layer formed on the surface, below which the original material is perfectly preserved. Numerical simulations allowed describing the flow field around the samples and characterizing the materials behavior, in terms of thermal conductivity, catalycity and oxidation effects at high enthalpies.

Keywords: A. Ceramic matrix composites; A. Zirconium; B. SEM; B. Modelling studies; C. Oxidation; C. High temperature corrosion

Declaration of interest: none.

1. Introduction

Thermal Protection Systems (TPS) in hypersonic vehicles call for a unique combination of properties required to withstand the challenges of extremely demanding aero-thermo-dynamic conditions in harsh environments, including hypersonic Mach numbers, temperatures above 2000°C, the activation of gas dissociation/recombination reactions at

* *Corresponding author. E-mail:* stefano.mungiguerra@unina.it
Phone: +39 081 7682358

extremely low oxygen partial pressures, which can substantially enhance the heat flux on the exposed surface of the spacecraft [1, 2]. At present, Silicon-based ceramics (e.g. SiC) and protected C/C composites are the most widely employed solution as structural materials for space thermal protection systems, but they are able to withstand temperatures lower than ~2000 K [3, 4].

Ultra-High-Temperature Ceramics (UHTC) composites, based on transition metals carbides and diborides and silicon carbides are currently considered potentially viable candidate systems for these applications, thanks to their extremely promising characteristics, such as melting temperatures exceeding 3500 K, strength and oxidation resistance at temperatures over 2000°C [5, 6]. Scarce mechanical properties and vulnerability to extensive oxidation limit the applicability of single phase materials to actual thermal protection systems. The dispersion of SiC or other Silicon based ceramics, in the form of particles, short fibers or whiskers, in the main refractory phase is therefore frequently used to improve damage tolerance and oxidation resistance thanks to the formation of an oxide protective scale [7]. Due to the poor fracture toughness and thermal shock resistance of monolithic UHTC materials, research is currently oriented towards Carbon Fiber reinforced Ultra-High-Temperature Ceramic Matrix Composites (UHTCMC), consisting of carbon fibers embedded in a UHTC-matrix, with the aim of developing large ultra-refractory components with enhanced mechanical properties and reliability for aerospace applications [8, 9].

Capability of surviving the exposition to harsh environments without significant oxidation/ablation is one of the key features of ceramic materials for TPS applications and a proper experimental characterization is needed in this sense. A primary evaluation of high-temperature ablation resistance can be performed by means of relatively cheap techniques like high power laser beams [10], plasma [11, 12] or oxyacetylene torch [13, 14, 15], which can produce significant heat fluxes on materials. However, as also suggested in [16], to test

the materials survivability in an environment representative of hypersonic flight conditions, a realistic combination of heat fluxes, pressures, flow velocity and chemical composition around the test articles needs to be reproduced. Therefore, the most recommended facilities for the characterization of aerospace ceramic materials in a relevant, simulated flight environment are hypersonic arc-jet wind tunnels [17, 18, 19].

The Horizon 2020 European C^{3}HARME research project, involving the University of Naples "Federico II" (UNINA) and the Institute of Science and Technology for Ceramics (ISTEC), is currently ongoing, focused on a new class of UHTCMCs for near zero-ablation thermal protection systems [20]. Small-sized samples, based on a ZrB_2-SiC matrix and Carbon fibers, were manufactured by ISTEC and tested in the UNINA arc-jet wind tunnel in stagnation-point configuration, where atmospheric re-entry conditions are reproduced at maximum flow total enthalpies higher than 20 MJ/kg, supersonic Mach number and temperatures over 2000°C in a gas atmosphere with high concentration of atomic oxygen. Non-intrusive diagnostic equipment, including a two-color pyrometer and an infrared thermo-camera, was employed to monitor the surface temperature of the samples. Post-test inspections were carried out to analyze the microstructures of the samples after the exposition to the aero-thermo-chemically aggressive flow. The experimental activities were supported by Computational Fluid Dynamics simulations. Proper numerical models were defined and employed to accurately predict not only the thermo-fluid-dynamic flow field around the test articles, but also the thermal behavior of the materials samples, including an investigation of the effect of material surface properties, such as emissivity, thermal conductivity and catalycity.

2. Materials and methods

2.1. Manufacturing of UHTCMC samples

Two discs of Ultra-High-Temperature Ceramic Matrix Composites were manufactured, with ~50 vol%- UHTC matrix (90 vol% ZrB_2 and 10 vol% SiC), and ~50 vol% coated carbon fibers, with a 0°/90° architecture, according to previous papers [21, 22, 23].

Commercial powders were used for the materials preparation: ZrB_2 (Grade B, H.C. Starck, Germany), specific surface area 1.0m^2/g, particle size range 0.5–6 μm, D_{50} 2.3 μm, impurities (wt.%): 0.09 C, 0.8 O, 0.19 N, 0.10 Fe, 1.82 Hf; Alpha phase SiC (Grade UF-25,H.C. Starck, Germany) specific surface area 23–26m^2/g, particle size range 0.35–1 μm, D_{50} 0.65 μm, impurities (wt.%): O:2.5, Fe:0.05, Al:0.04; Ca:0.01; PAN-derived carbon fiber (T800HB-PyC, Toray, Japan). ZrB_2 and SiC ceramic powders were mixed by wet ball-milling. With this mixture, aqueous slurries were prepared and used to infiltrate Cf layers that were subsequently stacked in a 0°/90° configuration and hot pressed according to previous studies [21, 22].

From the sintered discs, two button-shape coupons were machined with a 4mm-thick head, 17 mm diameter and an overall length of 11 mm including the cylindrical rear pin. Both samples had sharp edges on the front surface. The geometry is shown in Figure 1a. From now on, the two samples will be referred to as Sample n.1 and Sample n.2.

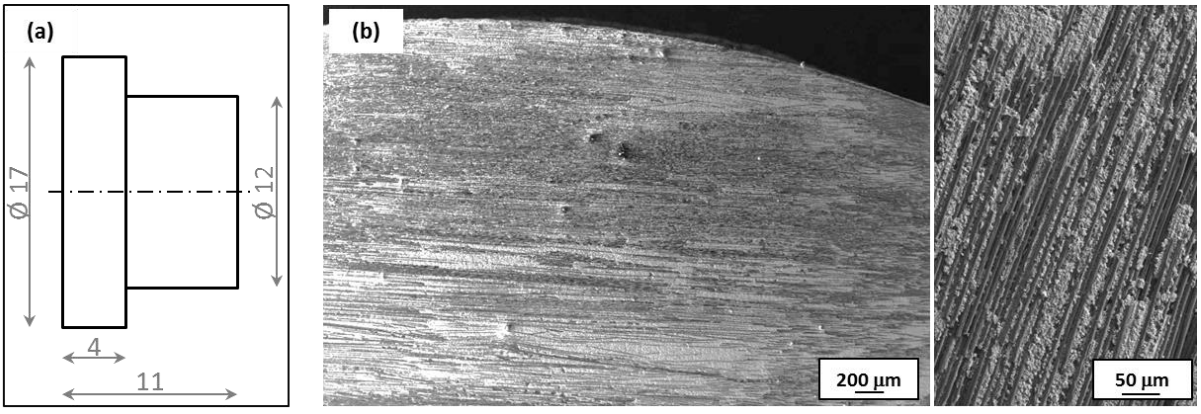

Figure 1: a) Drawing of the UHTCMC buttons tested in arc-jet wind tunnel and b) pristine surface of the UHTCMC Samples.

2.2. The arc-jet facility

Experimental tests were carried out in a continuous, open-circuit, blow-down arc-jet wind tunnel. An industrial torch is employed to produce nitrogen plasma and a mixer downstream supplies oxygen as secondary gas in order to simulate earth atmosphere. Tests are usually divided into steps, each one corresponding to an increase in the arc power of the torch, which leads to an increase in the temperature. The convergent-divergent conical nozzle is characterized by a throat diameter of 11 mm and an outlet diameter of 22 mm and is able to accelerate the flow up to a nominal Mach number about 3. The specific total enthalpy at the nozzle exit (H_0) is evaluated through an energy balance, with an overall uncertainty between 10 and 15%, as described in [24].

A dedicated, thermally protected supporting system is employed to place the samples inside the wind tunnel test chamber, at a distance of 1 cm from the supersonic nozzle outlet section.

The facility is provided with a two-color pyrometer and a thermo-camera for non-intrusive temperature measurements. In particular, the surface temperature of the samples can be continuously measured (±1% instrumental accuracy), in the range 1273-3273 K, by a digital pyrometer (Infratherm ISQ5, Impac Electronic GmbH, Germany) at an acquisition rate of 100 Hz. It can be operated in the two-color mode, combining the infrared responses of the material surfaces in the two overlapping infrared wavelength bands at 0.7–1.15 μm and 0.97–1.15 μm, to measure the actual temperature, independent on the spectral emissivity (ε_λ). Moreover, an infrared (IR) thermo-camera (TC, Pyroview 512N, DIAS Infrared GmbH, Germany), observing the sample side opposite to that monitored by the pyrometer, provides the thermal distribution on the material surface (±1% of measured value in °C at temperatures lower than 1400°C; ±2% at temperatures higher than 1400°C). The IR-TC measurement is dependent on the spectral emissivity (in the operating wavelength band, 0.8-1.1 μm), which

can in general change during tests due to surface chemical reactions. The problem is overcome matching the two instruments measurements, assuming that the spectral emissivity is constant in the considered wavelength band, temperature range and over the whole observed surface, in order to rebuild the overall temperature distribution.

2.3. Characterization

The microstructure before and after torch test was analyzed on the surface and section by scanning electron microscopy (FE-SEM, Carl Zeiss Sigma NTS Gmbh, Oberkochen, DE) and energy dispersive x-ray spectroscopy (EDS, INCA Energy 300, Oxford instruments, UK).

Given the brittle nature of the oxide scale formed and its tendency to spall-off, the ablation resistance was evaluated in terms of thickness of residual unaffected composite, estimated on the polished cross section of the buttons.

2.4. Numerical models

In order to properly characterize the flow field inside the facility and to rebuild the thermal behavior of the samples, Computational Fluid Dynamics (CFD) simulations were performed.

A simplified 2D-axisymmetric computational domain, shown in Figure 2a, is employed to perform steady-state simulations of the high-enthalpy flow field inside the mixing chamber and supersonic nozzle. The Reynolds-Averaged Navier-Stokes equations are solved for a turbulent multi-reacting gas mixture with five species (i.e. O, O_2, NO, N and N_2), in chemical non-equilibrium. Finite rate chemical reactions are considered, with the reaction rate constants specified by the Arrhenius law. Viscosity, thermal conductivity and mass diffusivities of the gas species are derived from the kinetic theory of gases. A density-based, steady, axisymmetric formulation of the equations is solved in these assumptions.

Through an axial mass flow inlet, representing the exit section of the torch, the specified mass flow rate of the hot gas (N_2, red in Figure 2a) coming from the torch is injected into the domain. The gas total temperature and chemical composition are evaluated by means of the

NASA CEA (Chemical Equilibrium with Applications) software [25] in order to match the total specific enthalpy corresponding to the desired value of the torch arc power. Furthermore, a radial mass flow inlet is used to simulate the injection of the cold gas (O_2, blue in Figure 2a) in the mixing chamber.

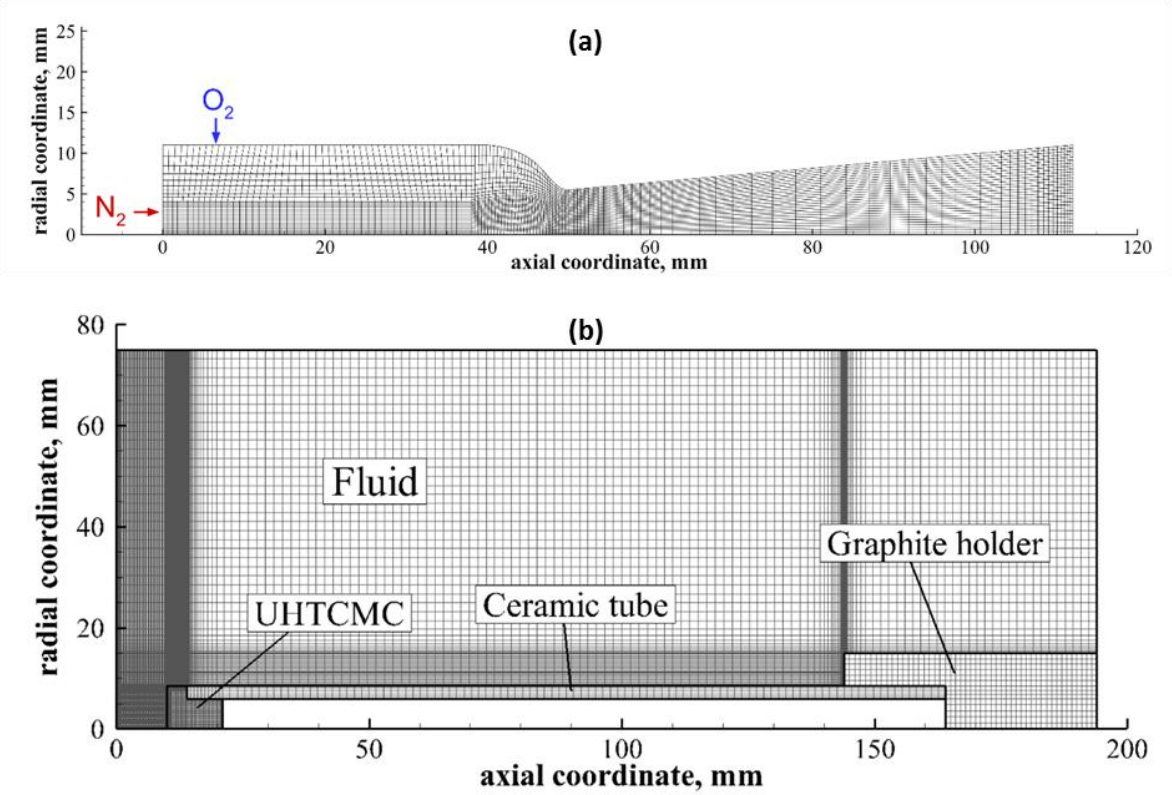

Figure 2: a) Computational domain for arc-jet facility CFD simulations and b) computational domain for the simulation of the test chamber flow field and the thermal analysis of the samples.

The thermo-fluid-dynamic conditions achieved at the nozzle exit section, corresponding to the inlet section of the test chamber, are then used as inputs to study the aero-thermo-dynamic flow field around the test article. Axisymmetric steady-state simulations are performed on a computational domain which includes both the fluid region of the test chamber and the solid components (Figure 2b). On the top and rear boundaries of the domain, a pressure-outlet condition corresponding to the experimental vacuum environment is set.

For the thermal analysis of the samples, the time-dependent temperature field inside the sample and its supporting elements can be computed solving the energy equation

$$(\rho C)_s \frac{\partial T}{\partial t} = k_s \nabla^2 T \quad (1)$$

where ρ_s, C_s and k_s are the solid density, specific heat and thermal conductivity, respectively.

The distribution of the thermo-fluid dynamic quantities and the chemical compositions in the fluid area near the solid material, and subsequently the convective heat flux, are influenced by the temperature on the exposed surface of the sample. For these reasons, an accurate approach is the one considering the interaction between the fluid and the materials. The thermal coupling condition is set on the interfaces between fluid and solid domains, that is temperature and heat flux continuities:

$$T_{f,int} = T_{s,int} \quad (2)$$

$$k_f \frac{\partial T}{\partial n}\Big|_{f,int} + \dot{q}_{rad,in} + \dot{q}_{chem} = k_s \frac{\partial T}{\partial n}\Big|_{s,int} + \dot{q}_{rad,out} \quad (3)$$

where n is the normal direction of the interface, the subscript f represents fluid, $\dot{q}_{rad,in}$ is the radiative heat flux entering the solid domain, $\dot{q}_{chem}$ is the chemical contribution to the heat transfer (due to the dissociation/recombination reactions occurring at the solid/fluid interface), $\dot{q}_{rad,out} = \varepsilon\sigma T^4$ is the radiative heat flux emitted by the solid surface.

2.4.1. Effect of the surface catalycity

Surface catalycity is defined as the ability of the material surface to promote exothermal recombination reactions at the wall. The diffusive flux of atomic species at the wall, part of which recombines into molecules, results in an increased heat flux, as shown in Eq. (3). According to [26], the diffusive flux at the wall for the i-th atomic species can be written as:

$$\frac{\partial C_i}{\partial n} = \frac{C_i K_w}{D_i} \quad (4)$$

where C_i is the species concentration, D_i the corresponding diffusivity and K_w is the material catalytic recombination rate constant, which is both function of the wall material and

on the considered chemical species. K_w can be expressed as function of the catalytic recombination coefficient γ_w:

$$K_w = \gamma_w \sqrt{\frac{R_0 T_w}{2\pi m_i}} \tag{5}$$

In Eq. (5), R_0 is the universal gas constant, T_w is the wall temperature and m_i is the molar mass of the i-th species. γ_w is the ratio between the number of atomic collisions effective in recombination and the total number of atomic collision occurring at the wall [27]. It can assume values between 0 and 1, being $\gamma_w = 0$ the case of not-catalytic wall (zero species diffusive flux) and $\gamma_w = 1$ the case of fully catalytic wall (zero atomic species concentration at the wall).

In the CFD simulation, it is possible to assign a specified value of the species concentration at the wall. Extracting, from the fluid field solution, the quantities appearing in Eqs. (4) and (5), the values of K_w and γ_w can be calculated. In the present work, to reduce the number of unknown quantities, it has been assumed that the catalytic recombination coefficients are the same for the two atomic species, nitrogen and oxygen.

3. Experimental results

The material final porosity was around 16%. The pristine surface of the samples is shown in Figure 1b.

Four tests were performed in the arc-jet facility described in Section 2.2. Sample n.1 was subjected to three heating cycles, reaching higher specific total enthalpies in each test, up to about 20 MJ/kg. Sample n.2 was only tested once, and a specific total enthalpy of 20 MJ/kg was reached also in this case. The enthalpy was increased stepwise, according to the levels reported in Table 1. In all the tests, an air mass flow rate of 1 g/s was set, with 0.2 oxygen and 0.8 nitrogen mass fractions.

Step	0	1	2	3	4	5	6	7	8
H_0 [MJ/kg]	5.5	7.0	8.5	10	12	14	16	18	20

Table 1: Specific total enthalpies at different steps during the tests.

3.1. Test on Sample n.1

Figure 3a shows the thermal histories of Sample n.1 in the different tests. The steps are numbered according to the specific total enthalpies achieved, summarized in Table 1. The measurements obtained by means of the two-color pyrometer (continuous lines) and the infrared thermo-camera (dotted lines) are compared, allowing an estimation of the surface spectral emissivity of the sample. Test 1 was a preliminary test, carried out a relatively low enthalpies, to assess the capability of the material to withstand exposure to supersonic plasma flow without significant damages. In Test 2, higher enthalpy levels were reached, achieving temperatures up to 2020 K. The spectral emissivity appears to be decreasing with temperature, possibly also because of the surface modification occurring during the exposure to plasma jet. The temperature measured by the thermo-camera is in fact shown in the assumption of a constant spectral emissivity of 0.75 [28] but it does not perfectly overlap the actual surface temperature measured by the pyrometer, in the two-color mode. Employing the procedure outlined in Section 2.2, it was possible to estimate that the spectral emissivity of the sample decreased from a value of 0.85 during the first two steps (specimen temperatures up to 1600 K), to 0.75 at the third step (temperature around 1700 K), to 0.6 during the fourth step and 0.5 for the fifth step, when the temperature exceeded 2000 K. This behavior is in line with literature data [29, 30] and the value of 0.5 is typical for zirconium oxide/silicon oxide outer scale [31]. The surface modifications are highlighted by the white color assumed by the sample head, as clearly visible in Figure 4a-c), showing the specimen before and after the tests. After the exposure to the first two heating cycles, however, the sample exhibited neither structural damages, nor significant mass losses.

Hence, it was possible to expose it to the arc-jet during a third test, reaching, as anticipated, a specific total enthalpy of the flow of 20 MJ/kg and temperatures higher than 2400 K. Once again, the decrease in spectral emissivity with temperature is noticeable, since the thermo-camera (dotted) curve is plotted in the assumption of $\varepsilon_\lambda = 0.75$. It is interesting to notice the appearance of a high-temperature spot on the front surface of the sample, highlighted in Figure 3b, which shows the infrared thermal images detected by the thermo-camera during Steps 5 and 8. The sample temperature in Step 5 is rather uniform, around 2000 K, except for the zone where the sample appears red, corresponding to a temperature of more than 2100 K. The hot spot is clearly visible until the end of the test, as demonstrated by the second thermal image of Figure 3b, where the presence of a thin layer relatively hotter than the rest of the sample surface is observable. As will be further discussed in the Sections dedicated to the SEM microstructural characterization and the numerical simulations, this behavior could be related to the formation of a zirconium oxide layer, leading to a dramatic reduction of the material thermal conductivity, which however preserves the rear part of the sample at sustainable temperatures. From Figure 4d), which depicts the sample after Test 3, it is possible to observe the tendency of the oxide to spall off, since a structural crack is evidently noticeable. This could justify the presence of the localized hot spot discussed above.

3.1. Test on Sample n.2

Sample n.2 was tested once, reaching the enthalpy levels corresponding to Steps from 1 to 8, listed in Table 1. The last step ($H_0 = 20$ MJ/kg) lasted about 120 s. The thermal history of the specimen is plotted in Figure 5, comparing the real temperature measurement performed by the pyrometer and the thermo-camera output, obtained assuming a constant spectral emissivity of 0.5. A slightly different positioning of the thermo-camera allowed in this case to observe also the front surface of the sample.

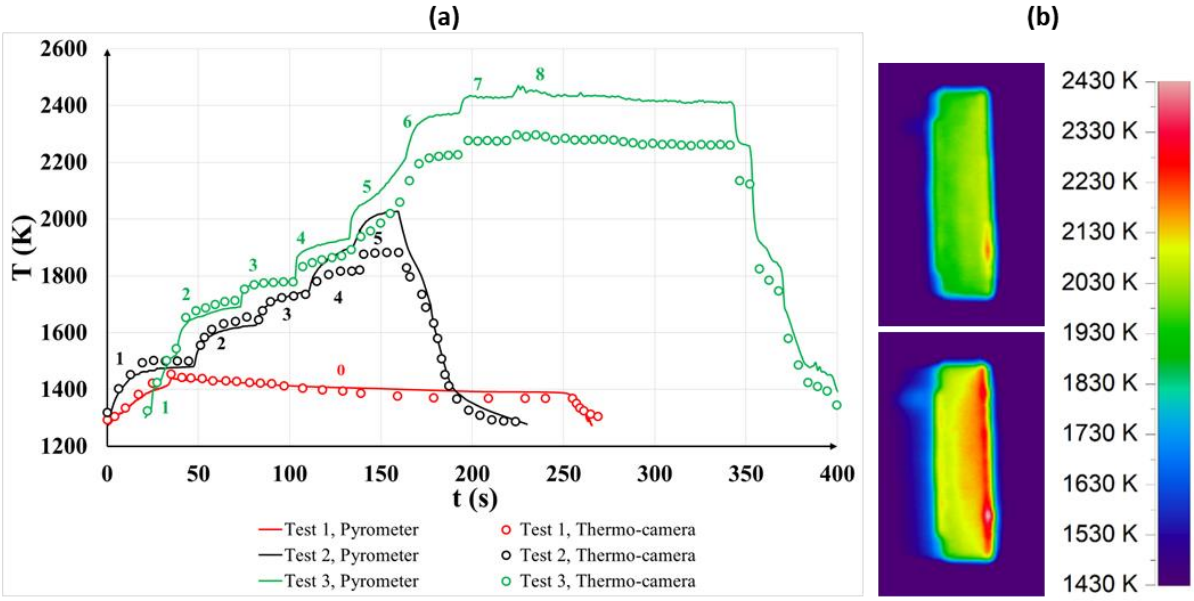

Figure 3: a) Time histories of the maximum surface temperature of Sample n.1 during the three arc-jet tests, comparison between pyrometer and thermo-camera measurements. The specific total enthalpy levels corresponding to each step are listed in Table 1. b) IR thermal images of Sample n.1 at Step 5 (top) and Step 8 (bottom) of Test 3.

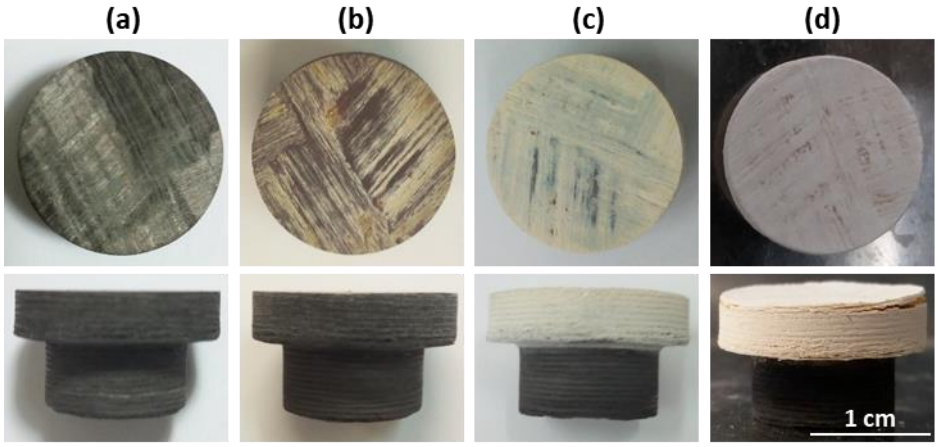

Figure 4: Pictures of Sample n.1 (a) before the tests, (b) after Test 1, (c) after Test 2, (d) after Test 3.

An interesting phenomenon was detected during the last step, when the thermo-camera signal presents a sudden discontinuity in the measured temperature (in Figure 5, it is highlighted by a red circle), similar to those detected during arc-jet characterization of ZrB_2-SiC UHTCs [24] and C-SiC composites [32]. This "*jump-of-radiance*" was associated to the appearance of some surface instabilities on the front face of the sample. Figure 5 also shows two thermal images of the sample, just before and just after the jump in the measured temperature. In the second picture, higher values of the irradiated power are noticeable in a bubble forming on the surface, due either to a reduction in spectral emissivity or to an

increase in temperature. In the second case, since the two-color pyrometer did not detect significant temperature jumps during the test, a possible explanation of this might be that the instrument, facing the opposite side of the sample, did not point directly on the instabilities. The formation of bubbles evolved unsteadily during the last enthalpy step, until a thin hot layer was formed also in this case in the front part of the sample, as shown in Figure 6. In the picture on the right, in particular, the front surface of the sample, relatively hotter than the rear region, is clearly distinguishable. According to the thermo-camera measurements, the highest temperature reached on the sample was almost 2550 K.

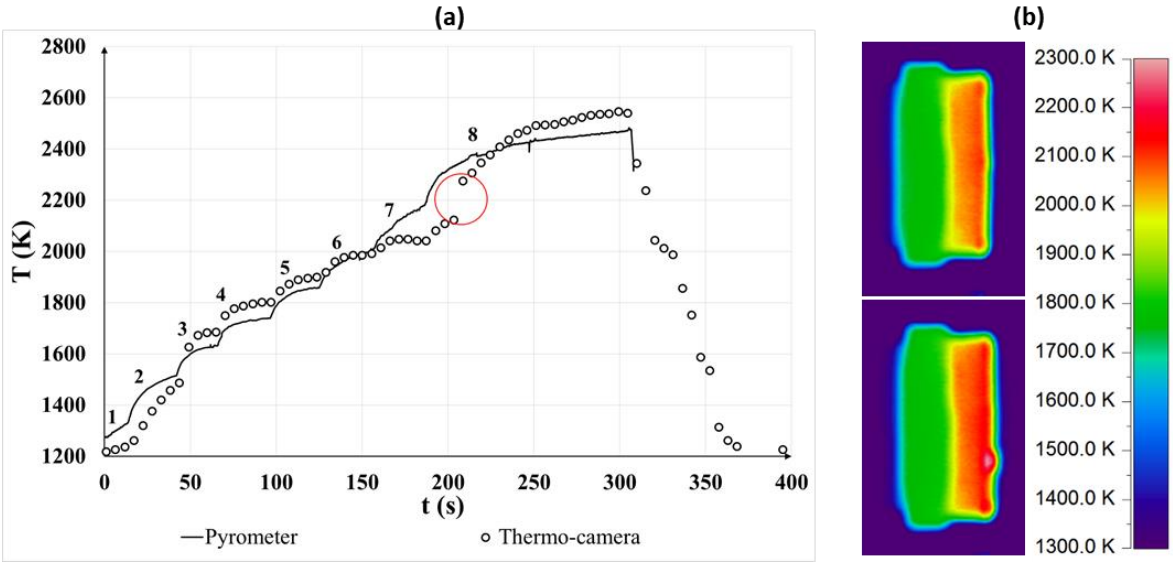

Figure 5: a) Time history of the temperature of Sample n.2 with comparison between pyrometer and thermo-camera data. The temperature profile of the thermo-camera is obtained under the hypothesis of a spectral emissivity of 0.5. The red circle highlights a "jump-of-radiance" detected by the thermo-camera during the final step. b) IR thermal images of the sample just before (above) and just after (below) the appearance of the jump-of-radiance.

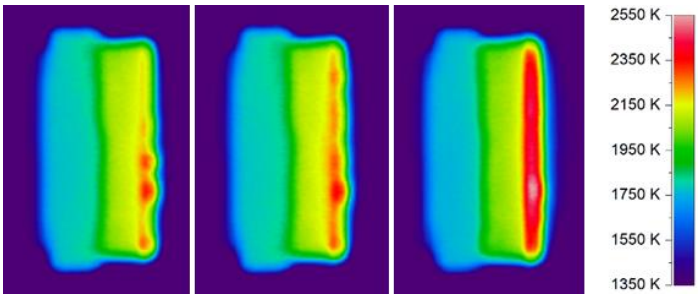

Figure 6: Thermal images of the evolution of surface instabilities on Sample n.2 during Step 8.

Bubble nucleation might be explained with extrusion of volatile products (e.g. CO, SiO, produced at high temperatures after transition from passive to active oxidation of SiC)

through the liquid film of SiO_2 covering the surface, until almost total removal of the glassy phase, which left exposed a zirconium dioxide layer, according to the typical oxidation mechanism of ZrB_2-SiC ceramics [33]. The ZrO_2 scale, as discussed for Sample n.1, is provided with insulating properties resulting in the temperature distribution observed by the IR thermal images, with the front, oxidized, area hotter than the rear bulk material.

3.2. Post-test microstructural characterization

Post-test analysis of the micro-structure of the samples after the exposition to the high-enthalpy flow was performed to evaluate the materials deterioration. Generally the microstructure evolution, phase composition and oxide architecture of the two model was alike, just the thickness of the oxide varied.

Figure 7 and Figure 8 show the surface appearance of the two samples. It appears evident that part of the outer oxide spalled off leaving exposed the material underneath, especially in Sample 1 which underwent harsher treatment (Figure 7). White zones are crystalline ZrO_2, whilst dark ones are a silica-based glass deriving from the oxidation of the initial SiC particles, Figure 7b. Carbon fibers are completely ablated from all the button surface and ZrO_2 in the center is coarse and partially melted, Figure 7c. The surface of Sample 2 (Figure 8) displays wider area of white ZrO_2, owing to limited oxide detachment.

The effect of single or multiple arc-jet wind tunnel exposure can be appreciated looking at the cross section of the buttons, Figure 9 and Figure 10, where material unaffected by the oxidation is marked: thickness is 3.20±0.06 mm for Sample 1 and 4.30±0.06 for Sample 2.

The elemental maps of boron, carbon, oxygen and silicon evidence that oxygen penetrated inside the sample of approximately 600 μm for Sample 1 and about 200 μm for Sample 2. The oxygen-rich areas are poor of boron, silicon and carbon, suggesting the layer is mainly made of zirconia. Below the oxide scale, the composition rapidly changes until the original bulk material is visible. The 0°/90° architecture of carbon fibers is still noticeable.

In both cases the outer oxide scale in the center is rather compact and partially detached from the underneath boride matrix and the magnified SEM images in Figure 11 highlight the oxide architecture, morphology and composition. Coarse ZrO_2 is found on the top with silica veins running along the grain for the whole thickness. Carbon fibers are completely removed and their place has been filled by growing oxide and liquid silica glass. The fibers re-appear only when the boride matrix is found un-attacked.

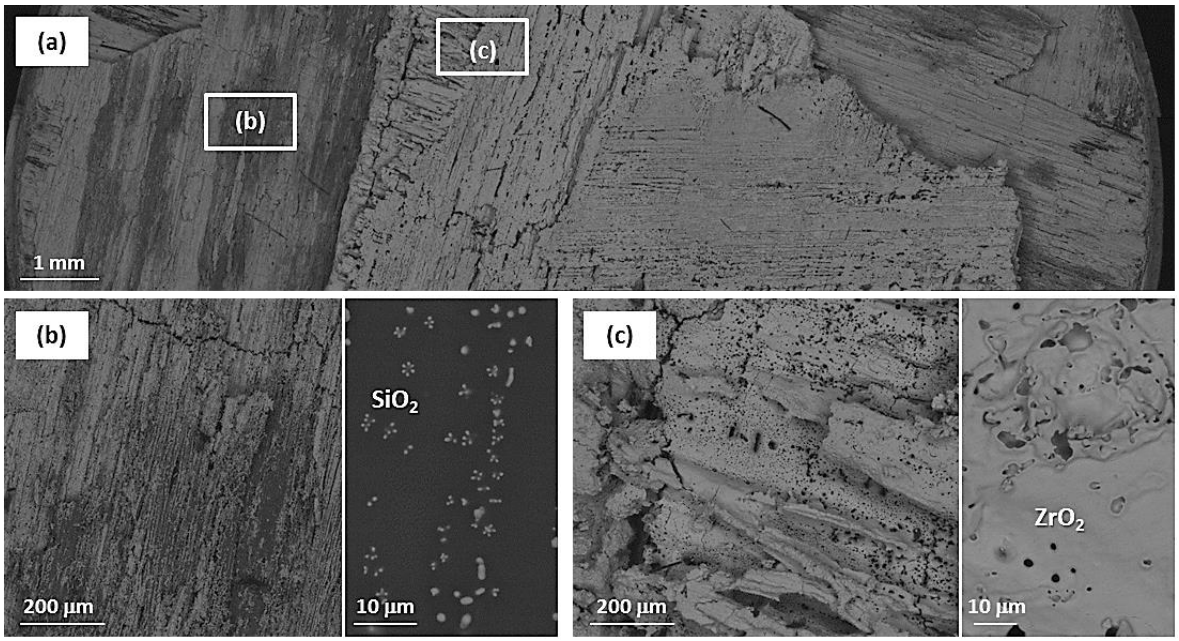

Figure 7: SEM images of the surface of Sample n.1 after Test 3 showing a) the overall appearance in the center of the button, b) the silica-rich areas left exposed upon oxide delamination and c) the outermost oxide.

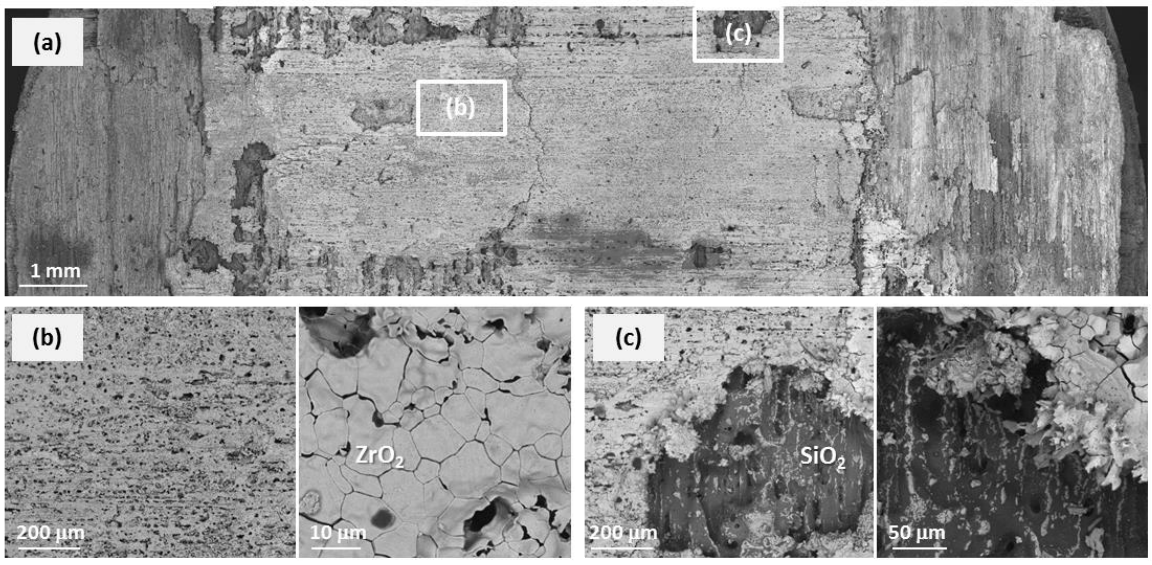

Figure 8: SEM images of the surface of Sample n.2 after arc jet test showing a) the overall of the button, b) the ZrO_2 aspect and c) silica-rich areas.

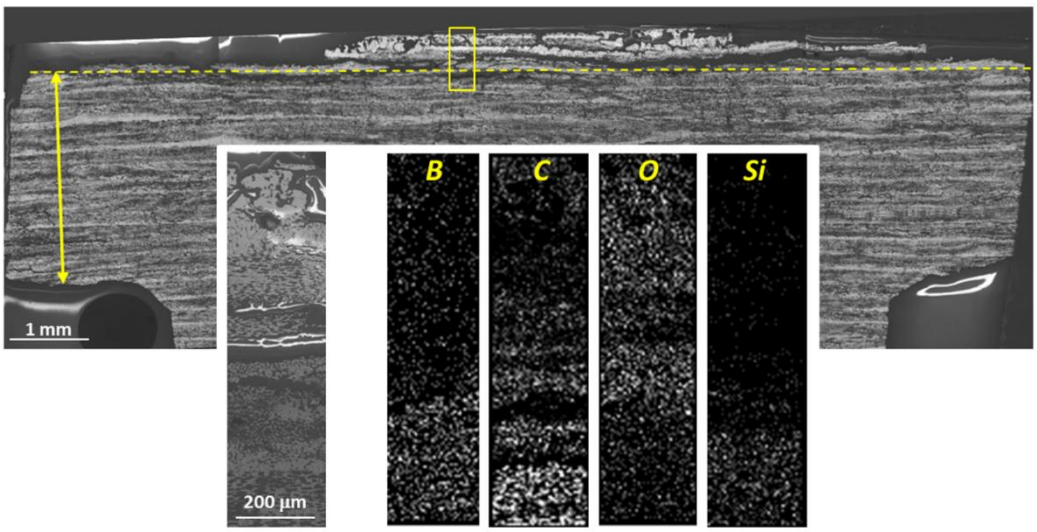

Figure 9: Cross-section of Sample n.1 upon Test 3 showing the oxide thickness, the residual unaffected material and the elemental maps distribution.

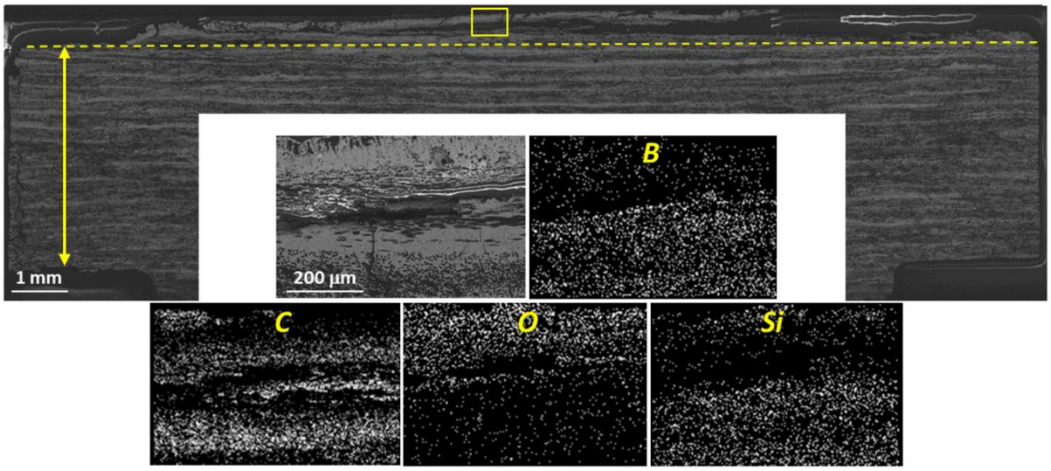

Figure 10: Cross-section of Sample n.2 upon Test, showing the oxide thickness, the residual unaffected material and the elemental maps distribution.

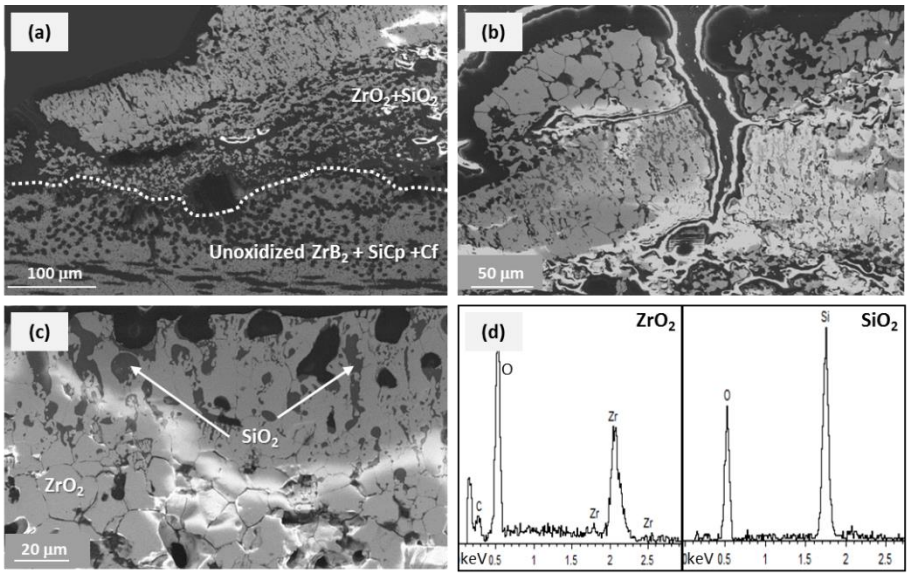

Figure 11: a)-c) SEM images of the cross section of Sample n.2 showing the oxide morphology, architecture and composition with EDS spectra in d).

4. Numerical simulations

Numerical simulations offer the possibility to rebuild the aero-thermo-dynamic conditions met by the samples in the test chamber and to characterize the unknown thermal and chemical properties of the material. In particular, it is interesting to investigate the effects of thermal conductivity and surface catalycity on the samples radiative equilibrium temperatures at different specific total enthalpy levels. Moreover, the outcomes of the samples microstructural characterization discussed in Section 3.2 can be used to investigate the effect of the presence of the zirconia layer during the final phases of test.

To achieve these objectives, some of the conditions of the experimental tests have been simulated by means of the CFD models presented in Section 2.4, studying both the high-enthalpy flow field and the thermal behavior of the samples. Different values of the torch arc power have been considered, corresponding to Steps 1, 3, 5 and 8 (Table 1). The simulation of the aero-thermo-chemical flow field in mixing chamber, nozzle and test chamber was coupled to the solution of energy equation inside the sample to characterize its thermal behavior. The results have been compared to the experimental measurements obtained for Sample n.1. The test on Sample n.2 was not considered because of the difficulty to properly model the thermo-chemical surface instabilities discussed in Section 3.1.

4.1. Simulation of the flow field in SPES

As an example, the Mach number distribution calculated inside the mixing chamber and nozzle of the arc-jet facility, for the case of Step 5 (H_0 = 14 MJ/kg), is depicted in Figure 12. As expected, a strong expansion occurs to the flow up to a Mach number value of almost 3 at nozzle exit. It resulted that higher values of the torch arc power lead not only to an increase in velocity, pressure and temperature at nozzle exit, but most of the specific total enthalpy is used to increase the mass fractions of the dissociated species (N and O). As discussed in next

Section, this is one of the reasons why surface catalycity becomes increasingly important at higher enthalpy levels.

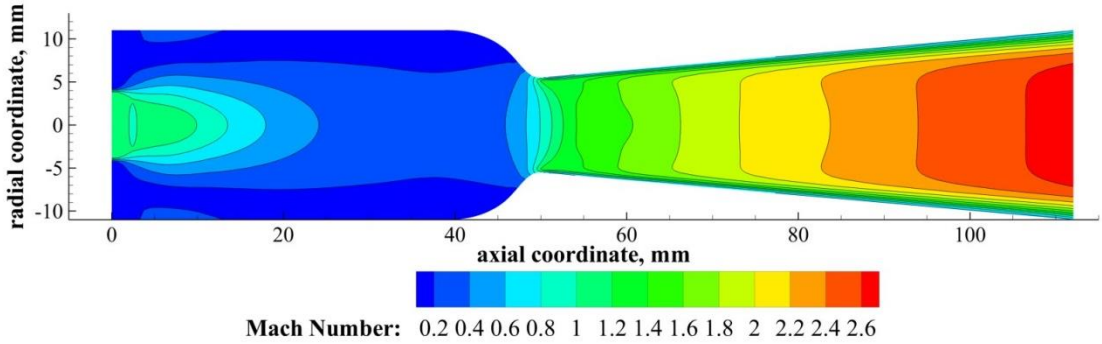

Figure 12: Mach Number distribution inside the mixing chamber and nozzle of the arc-jet facility. Conditions corresponding to Step 5 (H_0 = 14 MJ/kg).

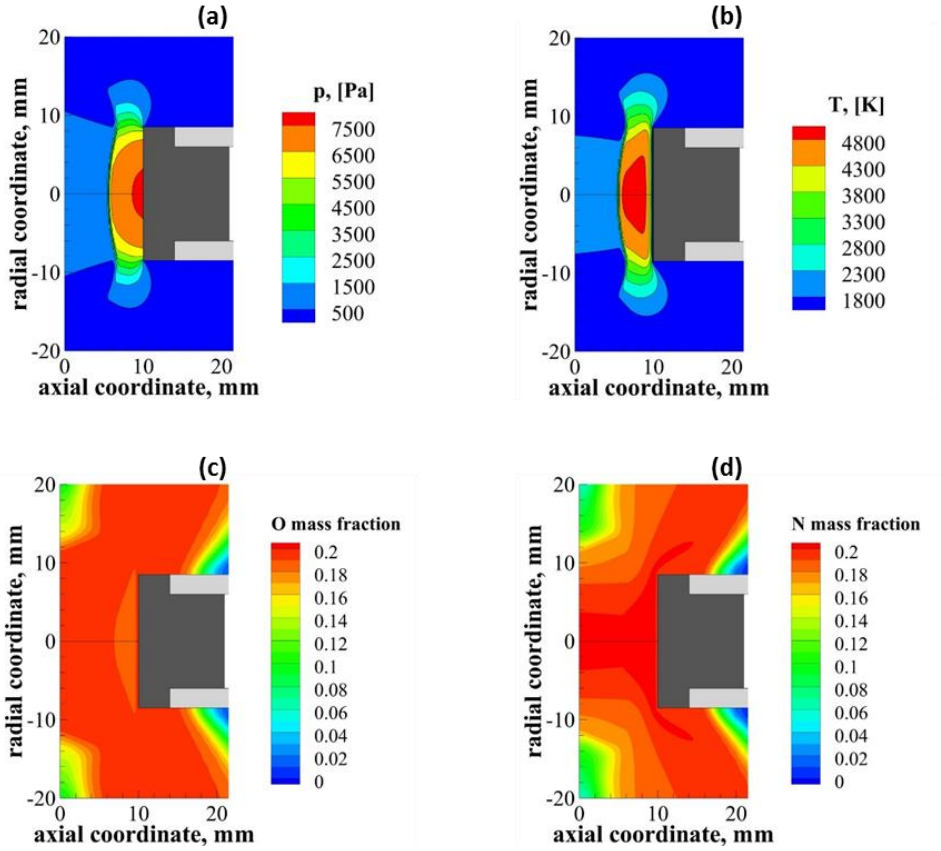

Figure 13: Distribution of a) static pressure, b) static temperature, c) O mass fraction and d) N mass fraction around the test sample. Conditions corresponding to Step 5 (H_0 = 14 MJ/kg).

The profiles of the thermo-fluid-dynamic quantities and of the species concentrations, obtained at nozzle exit, are used as inputs for the CFD simulation of the flow field inside the test chamber. As an example, Figure 13 shows the distributions of pressure, temperature and

atomic oxygen and nitrogen mass fractions around the sample obtained in correspondence of the enthalpy level of Step 5. It is clear that, even at intermediate enthalpies, there is a considerable amount of dissociated species, resulting in a not negligible effect of surface catalycity on sample equilibrium temperature. It is also interesting to notice that the λ-structure of the shock-wave that, according to CFD solution, forms in front of the sample, is clearly visible also in a picture taken by a CCD camera during the test (Figure 14).

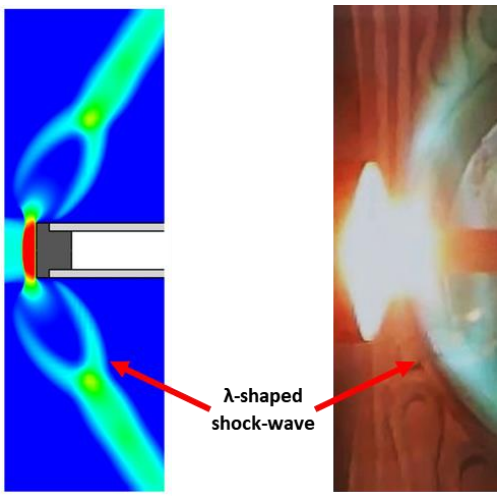

Figure 14: Comparison between numerical distribution of temperature (left) and a CCD picture of the test (right), which shows the λ-structure of the shockwave in front of the specimen.

Table 2 summarizes the average values of the surface heat flux obtained on the sample front surface at cold wall, in the hypothesis of zero catalytic activity. As discussed above, the increase in the enthalpy level only causes a slight rise in the flow static temperature at nozzle exit, whereas most of the energy is spent in the endothermal dissociation reactions of oxygen and nitrogen. Therefore, as reported in the Table, the heat flux only increases by less than 50% from Step 1 to 8, being in the order of 1-2 MW/m^2. As will be furtherly discussed, this is not sufficient to justify the rise in the sample equilibrium temperature, which is probably also related to modifications of the surface properties of the sample. In particular, besides the variation of surface emissivity already discussed in Section 3.1, it will be necessary to suppose that the sample surface promotes a partial catalytic recombination of oxygen and nitrogen dissociated atoms into molecules.

A detailed analysis of the effect of surface catalycity on radiative equilibrium temperature was carried out for the conditions corresponding to Step 5. As shown in Table 3, in presence of a complete recombination of both the atomic species at the wall, the average heat flux at those conditions increases from 1.33 MW/m^2 up to 3.59 MW/m^2, whereas the maximum heat flux rises from 1.58 MW/m^2 to 4.50 MW/m^2. The actual value of surface heat flux, depending on the effective catalytic recombination efficiency, is expected for this reason to attain values in the interval defined by the two limit cases (not-catalytic and fully-catalytic).

Step	Average Surface Heat Flux [MW/m^2]	Maximum Surface Heat Flux [MW/m^2]
1	1.07	1.28
3	1.22	1.46
5	1.33	1.58
8	1.59	1.82

Table 2: Average and Maximum Heat Flux on the sample front surface at Cold, Not-Catalytic Wall, for the four analyzed enthalpy steps.

	Average Surface Heat Flux [MW/m^2]	Maximum Surface Heat Flux [MW/m^2]
Not-Catalytic	1.33	1.58
Fully-Catalytic	3.59	4.50

Table 3: Average and Maximum Heat Flux on the sample front surface at Step 5, comparison between Not-Catalytic and Fully-Catalytic Wall.

4.2 Thermal analysis of the solid sample

Coupled to the fluid field, the thermal behavior of the material has been studied, performing steady-state simulations. The results of the simulations corresponding to the enthalpy levels of Steps 1, 3 and 5 were compared to the experimental data measured during Test 2 on Sample n.1. To investigate the effect of the zirconia layer that formed on the front surface of the sample at high enthalpies, also the thermal behavior at Step 8 of Test 3 was simulated.

The density of the sample was derived from mass and volume measurements, and was equal to 3000 kg/m^3. The thermal conductivity was instead estimated by means of a

sensitivity analysis, comparing the CFD and experimental axial temperature profiles, as it will be shown in the following.

The material surface emissivity, as discussed in Section 3.1, changed during the different steps of Tests 2 and 3. Different values have for this reason been used in the different simulations. The values of the overall surface emissivity have been estimated based on the spectral emissivities derived from the IR-TC measurements, in the assumption that, at the high temperatures reached during the tests, most of the power is irradiated in the wavelength band around 1μm, where the value of ε_λ was calculated [34]: it is therefore reasonable to assume that the estimated value of spectral emissivity is representative of the total emissivity along the whole wavelength spectrum.

To evaluate the thermal conductivity of the sample, a sensitivity analysis was performed. Assuming a surface emissivity $\varepsilon = 0.9$ and a not-catalytic behavior, different CFD simulations were carried out to match the temperature axial profile obtained by means of the thermo-camera measurements, in the case of Step 1. As shown in Figure 15a, the value of $k = 20$ W/(m K) allows matching the experimental surface temperature slope along the axial direction. Hence, this value was used also for the simulations of Steps 3 and 5. Figure 15b and c shows also a comparison between the numerical and experimental distributions of temperature inside the sample.

To match the experimental values of maximum temperature at higher enthalpy levels at the steady state, both the conditions on surface emissivity and catalycity needed to be changed. In particular, based on the analysis of the spectral emissivity reported above, values of 0.75 and 0.5 were set for the total emissivity of the specimen, respectively for Step 3 and 5 of Test 2. However, the reduction in the irradiated power was not enough to justify the rise in temperature. To match the experimental value of the surface temperature, also catalycity needed to be taken into account.

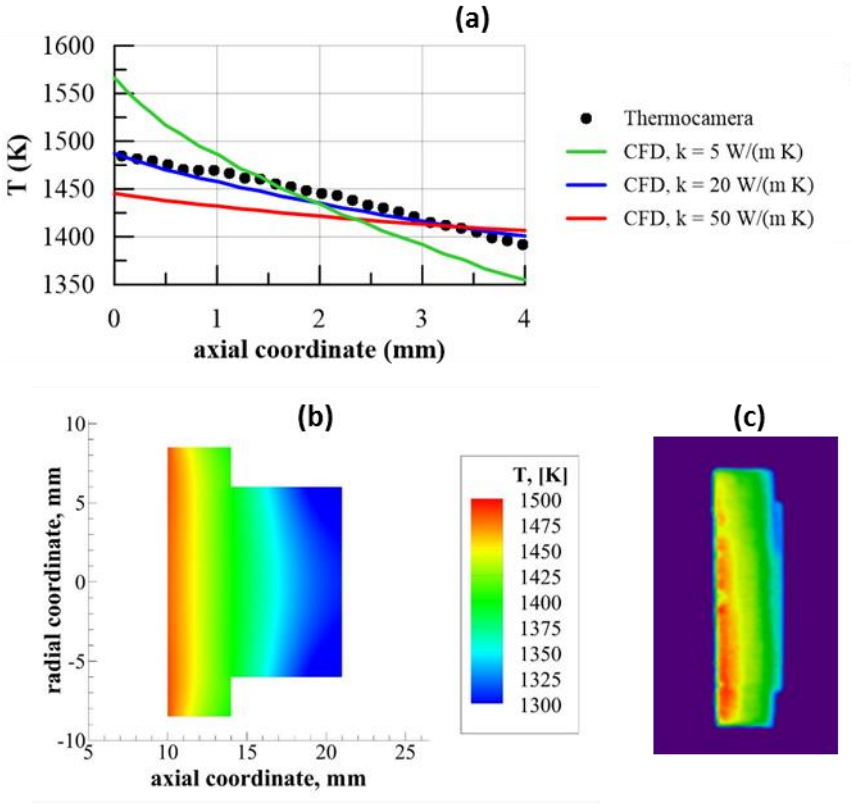

Figure 15: a) Experimental and numerical temperature axial profiles at steady state, for different values of the thermal conductivity. Conditions corresponding to Step 1 of Test 2 on Sample n.1 (H_0 = 7 MJ/kg). b) Temperature distribution inside the UHTCMC specimen: comparison between b) CFD steady-state solution and c) experimental measurement by IR thermo-camera.

Therefore, based on the model described in Section 2.4.1, a detailed parametric analysis on the effect of the catalytic recombination occurring at wall has been performed for Step 5. For different values of the catalytic recombination coefficient, ranging from zero- to fully-catalytic condition, steady simulations have been carried out. The resulting maximum sample temperature is reported versus γ_w in Figure 16. The diagram shows the typical s-shape also reported in [35,36]. Comparing the results of the simulations with the experimental data, it was possible to estimate the value of γ_w allowing to match the pyrometer measurement. In particular, the catalytic recombination coefficient γ_w was set to $5.5*10^{-3}$ and $8.5*10^{-3}$, respectively for Steps 3 and 5.

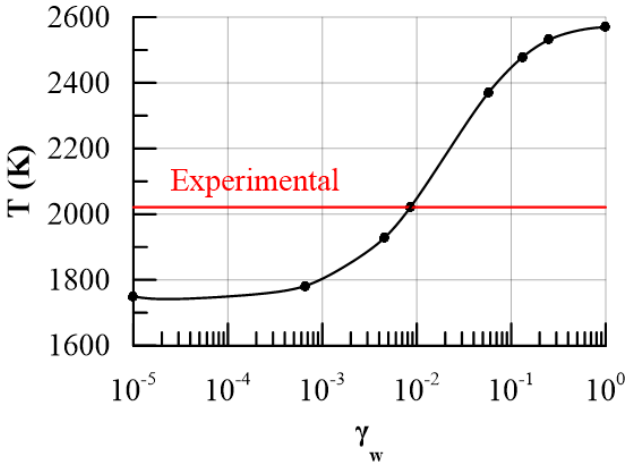

Figure 16: Maximum sample front surface temperature versus catalytic recombination efficiency, for Step 5 of Test 2 on Sample n.1 (H_0 = 14 MJ/kg, ε = 0.5).

Figure 17 shows a comparison between the numerical and experimental temperature axial profiles along the specimen for the three analyzed steps of Test 2. The curves confirm that there is a good agreement not only in the maximum value, but also in the slope along the axis, justifying again the choice of a thermal conductivity of 20 W/(m K).

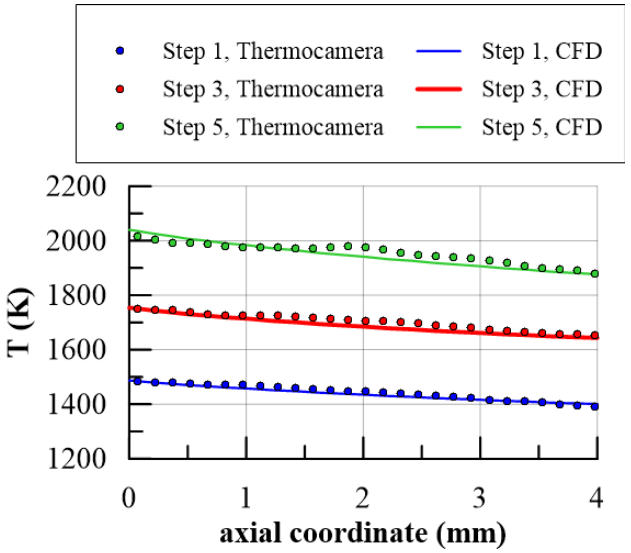

Figure 17: Comparison between experimental and numerical temperature axial profiles for the three analyzed steps of Test 2.

As discussed in Section 3.1, Sample n.1 experienced a localized rise in temperature, in the region close to the exposed surface. Based on the SEM cross-sections shown in Section 3.2, this phenomenon could be explained taking into account the formation of a zirconia layer, about 600 μm thick, characterized by a relatively low thermal conductivity. To assess this

hypothesis, one more CFD simulation was performed, including an oxidized region, with a thickness of 600 μm and a thermal conductivity of 2 W/(m K) [37, 38]. The surface emissivity was set to 0.5, the catalytic recombination efficiency γ_w was set to 10^{-2}, and the thermal conductivity in the unoxidized region of the sample was kept to the previously found value of 20 W/(m K). Figure 18 shows the comparison between the temperature axial profiles obtained by combination of pyrometer and thermo-camera measurements and rebuilt by CFD simulation, at steady state. An excellent match between the profiles is observable, showing that the temperature drops by about 200-300 K through the oxide layer, which plays the fundamental role of thermal barrier, preserving the rear region at sustainable temperatures and un-attacked by the aggressive aero-thermo-chemical environment.

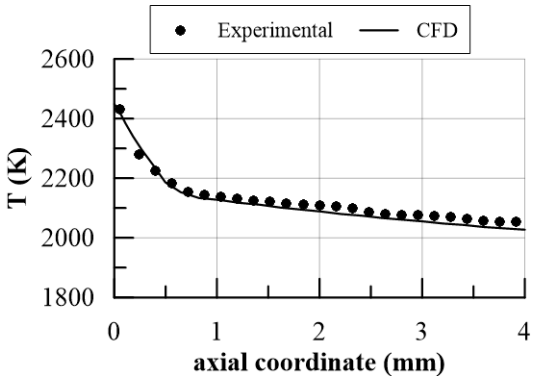

Figure 18: Comparison between experimental and numerical temperature axial profiles, at steady state, for Step 8 of Test 3 on Sample n.1 (H_0 = 20 MJ/kg).

5. Conclusions

In the present paper, Ultra-High-Temperature Ceramic Matrix Composite materials have been characterized in hypersonic arc-jet wind tunnel. Two small-sized samples, based on a ZrB_2-10% vol SiC matrix and Carbon fibers, with 0°/90° architecture, were manufactured and exposed to a supersonic plasma flow of simulated air, at specific total enthalpies up to 20 MJ/kg and surface heat fluxes in the order of 1-5 MW/m^2. The maximum surface temperature, measured by means of a two-color pyrometer and an infrared thermo-camera, exceeded 2400 K for both samples. Surface instabilities, associated to the appearance of

bubbles and to a *jump-of-radiance* detected by the thermo-camera, were observed at the maximum enthalpy level.

Post-test SEM and EDS analyses revealed the presence of a fiber-depleted zirconium oxide layer on the exposed surface of both the samples. The thickness of this layer is higher (about 600 μm) for Sample n.1, which was tested three times, at increasing maximum enthalpy levels, whereas it is about 200 μm for Sample n.2. In some areas, the fragile zirconium oxide detached from the sample, revealing silica glass regions. Below the oxide layer, the unoxidized bulk material is found perfectly preserved.

Computational Fluid Dynamics simulations were performed to evaluate the aero-thermo-dynamic conditions around the samples during the tests; a sensitivity analysis allowed estimating the thermal conductivity of the samples, matching experimental and numerical results. Moreover, the effect of surface catalycity was investigated, showing its importance at high enthalpies, when dissociation of nitrogen and oxygen is considerable. The insulating layer, formed on the exposed surface due to zirconium oxidation at ultra-high temperatures, in agreement with the numerical study, acts as a thermal barrier, leaving the back material at sustainable temperatures.

6. Acknowledgements

The C^3HARME research project has received funding by the European Union's Horizon2020 research and innovation programme under the Grant Agreement 685594.

D.S., A.V. and L.Z. wish to acknowledge A. Schoberth (AIRBUS), P. Meistring (AIRBUS), Felix Meistring (Arianegroup) for technical support.

Data availability

The raw/processed data required to reproduce these findings cannot be shared at this time due to technical or time limitations.

References

[1] W.G. Fahrenholtz, G.E. Hilmas, Ultra-high temperature ceramics: Materials for extreme environments, Scripta Materialia 129 (2017) 94-99.

[2] E. Wuchina, E. Opila, M. Opeka, W. Fahrenholtz, I. Talmy, UHTCs: Ultra-High Temperature Ceramic materials for extreme environment applications, Electrochem. Soc. Interface 16 (2007) 30-36.

[3] P. Sanoj, B. Kandasubramanian, Hybrid Carbon-Carbon Ablative Composites for Thermal Protection in Aerospace, J. Compos. 2014 (2014) 1-15.

[4] J. Zheng, H. Cui, H. Lib, Y. Li, D. Yao, Z. Ying, H. Deng, Mechanical and ablative properties of C/C composites modified by SiC using liquid silicon infiltration method, 68th International Astronautical Congress, Adelaide, Australia, September 2017.

[5] E. P. Simonenko, et al., Promising Ultra-High-Temperature Ceramic Materials for Aerospace Applications, Rus. J. Inorg. Chem. 58 (14) (2013) 1669–1693.

[6] L. Silvestroni, H-J. Kleebe, W.G. Fahrenholtz, J. Watts Super-strong materials for temperatures exceeding 2000°C, Sci. Rep. 7 (2017), 40730, doi: 10.1038/srep40730.

[7] T.A. Parthasarathy, D. Petry, M.K. Cinibulk, T. Mathur, M.R. Mark, R. Gruber, Thermal and Oxidation Response of UHTC Leading Edge Samples Exposed to Simulated Hypersonic Flight Conditions, J. Am. Ceram. Soc. 96 (3) (2013) 907-915.

[8] S. Tang, C. Hu, Design, Preparation and Properties of Carbon Fiber Reinforced Ultra-High Temperature Ceramic Composites for Aerospace Applications: A Review, J. Mater. Sci. Technol. 33 (2) (2017) 117-130, doi: 10.1016/j.jmst.2016.08.004.

[9] D. Sciti, L. Zoli, L. Silvestroni, A. Cecere, G.D. Di Martino, R. Savino, Design, fabrication and high velocity oxy-fuel torch tests of a Cf-ZrB2-nozzle to evaluate its potential in rocket motors, Mat. Des. 109 (2016) 709–717.

[10] W.E. Lee, E. Eakins, H. Jackson, D. Jayaseelan, Advanced characterization of composite ultra high temperature ceramic systems, in: W. Fahrenholtz, W. Lee, E.J. Wuchina, Y. Zhou, Ultra-High Temperature Ceramics: Materials For Extreme Environmental Applications II, Aerospace Research Institute Eds, ECI Symposium Series, 2013.

[11] A. Nisar, S. Ariharan, T. Venkateswaran, N.Sreenivas, K. Balani, Oxidation studies on TaC based ultra-high temperature ceramic composites under plasma arc jet exposure, Corros. Sci. 109 (2016) 50-61.

[12] L. Scatteia, D. Alfano, S. Cantoni, F. Monteverde, A. Di Maso, M. De Stefano Fumo, Plasma Torch Test of an Ultra-High-Temperature Ceramics Nose Cone Demonstrator, J. Spacecr. Rock. 47 (2) (2010) 271-279.

[13] A. Paul, J.G.P. Binner, B. Vaidhyanathan, A.C.J. Heaton, P.M. Brown, Oxyacetylene torch testing and microstructural characterization of tantalum carbide, J. Microsc. 250 (2) (2013) 122-129.

[14] M. Natali, M. Monti, J.M. Kenny, L. Torre, A nanostructured ablative bulk molding compound: Development and characterization, Compos. Pt A Appl. Sci. Manuf. 42 (9) (2011) 1197-1204.

[15] S. Zhou, W. Li, P. Hu, L. Weng, Ablation Behavior of ZrB_2–SiC–ZrO_2 Ceramic Composites by Means of the Oxyacetylene Torch, Corros. Sci. 51 (9) (2009) 2071-2079.

[16] T.A. Parthasarathy, M.K. Cinibulk, M. Opeka, Modeling and evaluating the environmental degradation of UHTCs under hypersonic flow, in: W. Fahrenholtz, E. Wuchina, W. Lee, Y. Zhou (Eds.), Ultra-High Temperature Ceramics: Materials for Extreme Environment Applications, First ed., John Wiley & Sons, Inc., 2014, pp. 268–290.

[17] A. Purwar, V. Thiruvenkatam, B. Basu, Experimental and computational analysis of thermo-oxidative-structural stability of ZrB_2–SiC–Ti during arc-jet testing, J. Am. Ceram. Soc. 100 (10) (2017) 4860-4873.

[18] P.J. Ritt, P.A. Williams, S.C. Splinter, J.H. Perepezko, Arc jet testing and evaluation of Mo–Si–B coated Mo and SiC–ZrB2 ceramics, J. Eur. Ceram. Soc. 34 (15) (2014) 3521-3533.

[19] F. Monteverde, D. Alfano, R. Savino, Effects of LaB_6 addition on arc-jet convectively heated SiC-containing ZrB2-based ultra-high temperature ceramics in high enthalpy supersonic airflows, Corros. Sci. 75 (2013) 443-453.

[20] C3HARME Project Website: https://c3harme.eu/.

[21] L. Zoli, V. Medri, C. Melandri, D. Sciti, Continuous SiC fibers-ZrB_2 composites, J. Eur. Ceram. Soc. 35 (2015) 4371-4376.

[22] D. Sciti, A. Natali Murri, V. Medri, L. Zoli, Continuous C fibre composites with a porous ZrB_2 Matrix, Mater. Des. 85 (2015) 127-134. doi:10.1016/j.matdes.2015.06.136.

[23] L. Zoli, D. Sciti, Efficacy of a ZrB_2–SiC matrix in protecting C fibres from oxidation in novel UHTCMC materials, Mater. Des. 113 (2017) 207–213. doi:10.1016/j.matdes.2016.09.104.

[24] F. Monteverde, A. Cecere, R. Savino, Thermo-chemical surface instabilities of SiC-ZrB_2 ceramics in high enthalpy dissociated supersonic air flows, J. Eur. Ceram. Soc. 37 (6) (2017) 2325-2341.

[25] S. Gordon, B.J. McBride, Computer Program of Complex Chemical Equilibrium Compositions and Applications, NASA Reference Publication 1311, 1994.

[26] O.N. Suslov, G.A. Tirskiy, The kinetics of the recombination of nitrogen atoms on high temperature reusable surface insulation in hypersonic thermo-chemical non-equilibrium flow, 2nd European Symposium on Aerothermodynamics for Space Vehicles, Noordwijk, The Netherlands, November 1994 (ESA SP-367, February 1995).

[27] S.M. Scala, Hypersonic Heat Transfer to Catalytic Surfaces, Ramo-Wooldridge Second Symposium on Ballistic Missiles, Los Angeles, California, June 1957.

[28] M. Balat-Pichelin, E. Bêche, D. Sciti, D. Alfano, Emissivity, catalycity and microstructural characterization of ZrB2–SiCfiber based UHTC at high temperature in a non-equilibrium air plasma flow, Ceram. Int. 40 (7), Part A (2014) 9731-9742.

[29] Y.S. Touloukian, D.P. DeWitt, Thermophysical properties of matter – The TPRC Data Series, Vol. 8, Thermal radiative properties: nonmetallic solids, IFI/Plenum, New York – Washington, 1972.

[30] G.T. Van Laningham, Oxidation resistance, thermal conductivity, and spectral emittance of fully dense zirconium diboride with silicon carbide and tantalum diboride additives, PhD Thesis, Georgia Institute of Technology, May 2012.

[31] D. Sciti, R. Savino, L. Silvestroni, Aerothermal behaviour of a SiC fibre-reinforced ZrB_2 sharp component in supersonic regime, J. Eur. Ceram. Soc. 32 (8) (2012) 1837–1845, doi: 10.1016/j.jeurceramsoc.2012.01.019.

[32] M. Balat-Pichelin, L. Charpentier, F. Panerai, O. Chazot, B. Helber, K. G. Nickel, Passive/active oxidation transition for CMC structural materials designed for the IXV vehicle reentry phase, J. Eur. Ceram. Soc. 35 (2) (2015) 487-502.

[33] T.A. Parthasarathy, R.A. Rapp, M. Opeka, M.K. Cinibulk, Modeling Oxidation Kinetics of SiC-Containing Refractory Diborides, J. Am. Ceram. Soc. 95 (1) (2012), 338-349.

[34] R. Siegel, J.R. Howell, Thermal radiation heat transfer, Taylor & Francis, Inc., New York, 1978.

[35] C.D. Scott, Catalytic Recombination of Nitrogen and Oxygen on High-Temperature Reusable Surface Insulation, AIAA 15th Thermophysics Conference, Snowmass, Colorado, July 1980.

[36] R. Goulard, On Catalytic Recombination Rates in Hypersonic Stagnation Heat Transfer, Jet Prop. 28 (1958) 737-745.

[37] Z. Deng, J.M.F. Ferreira, Y.Tanaka, Y. Isoda, Microstructure and thermal conductivity of porous ZrO_2 ceramics, Acta Materialia 55 (11) (2007) 3663-3669.

[38] K.W. Schlichting, N.P. Padture, P.G. Klemens, Thermal conductivity of dense and porous yttria-stabilized zirconia, J. Mater. Sci. 36 (2001) 3003-3010.